Comparison of the Mid-Infrared Magneto-Optical Response of $Ga_{1-x}Mn_xAs$ Films Grown by Molecular Beam Epitaxy and Ion Implantation and Pulsed Laser Melting

**G. Acbas · J. Sinova · M.A. Scarpulla · O.D. Dubon ·
M. Cukr · V. Novak · J. Cerne**

Abstract We have carried out mid-infrared magneto-optical studies of $Ga_{1-x}Mn_xAs$ films grown using two different techniques: low temperature molecular beam epitaxy (LT-MBE) and a combination of ion-implantation and pulsed laser melting (II-PLM). The second method is a high temperature growth technique which minimizes the formation of Mn interstitials. Both samples exhibit a ferromagnetic response with similar Curie temperatures (T_C). The samples show qualitatively similar behavior in below bandgap Faraday and Kerr measurements, which probe the valence band structure of the materials. This suggests that the same mid-infrared transitions are dominating the magneto-optical response of both samples.

G. Acbas (✉) · J. Cerne
Physics Department, University at Buffalo, SUNY, Buffalo, USA
e-mail: gacbas@buffalo.edu

J. Sinova
Physics Department, Texas A&M University, College Station, USA

M.A. Scarpulla
Materials Department, University of California, Santa Barbara, USA

O.D. Dubon
Material Science and Engineering Department, University of California, Berkeley, USA

M. Cukr · V. Novak
Institute of Physics, Acad. of Sciences of the Czech Republic, Prague, Czech Republic

1 Introduction

GaMnAs is the most studied III-V diluted magnetic semiconductor. However, the detailed band structure is not known and different experiments suggest different scenarios (see [1] for a recent review). This is in part due to the fact that the sample properties depend strongly on the growth and post-growth processes. For example, samples with the same magnetic ion concentrations and carrier density can have very different Curie temperatures.

It is acknowledged that the ferromagnetic exchange in GaMnAs is mediated by p-type carriers. The Mn dopants substitute for the cation site and supply a local magnetic moment, as well as acting as an acceptor providing holes that mediate the ferromagnetic order. However, Mn atoms can also act as double donors in interstitial sites, compensating p-type carriers and coupling antiferromagnetically with neighboring substitutional Mn atoms [2]. Other disorder effects are also present, notably As antisites, which were shown to strongly influence the magnetization.

Magneto-optical measurements (Magnetic Circular Dichroism and Kerr Effect) [3–6] at energies above the conduction band have been used to obtain information on the hole mediated exchange interaction between Mn ions, the spin-split bands, the magnetic anisotropies, and the presence of segregated second phases. Since they are the direct consequence of the giant spin splitting of the semiconductor band structure, these measurements showed that ferromagnetism is an inherent property of the zinc blende structure, and their features can be explained in terms of transitions between valence band and conduction band states assuming the Fermi level lies in the valence band and a dispersionless level is superimposed in the conduction band.

On the other hand, transmission and reflection measurements [7] at energies below the band gap, showed infrared

absorption energies shifting with carrier density in a way that suggests the presence of an impurity band formed by Mn acceptors.

Since the concentration of donor and acceptor dopants determines the population of ionized defects and thus influences the Fermi level, in this paper, we look at two samples grown by two different methods with different disorder effects, especially in the interstitial Mn concentrations.

2 Samples

One sample is a 50 nm thick GaMnAs film grown by low-temperature molecular beam epitaxy (LT-MBE) on a GaAs substrate ($x = 0.05$). The hole concentration of 2.5×10^{20} cm^{-3} is determined through DC Hall effect measurements at fields up to 9 T and at a temperature of 4 K. This hole density is estimated to be within 30% of the value that would be extracted from high field (30 T) measurements.

The other sample is grown by a combination of ion-implantation and pulsed laser melting (II-PLM) [8]. A semi-insulating GaAs wafer was implanted with Mn ions and then irradiated with a KrF laser causing the implanted layer to melt and crystallize upon solidification. Secondary ion mass spectrometry measurements indicate that the peak of the Mn distribution (which dominates the film properties) is about $x = 0.08$, while ion beam analysis (Rutherford Backscattering Spectrometry/particle induced X-ray emission, RBS/PIXE) indicates that ~80% of Mn is substitutional on Ga sites, reducing the effective Mn concentration to $x = 0.056$. The film effective thickness is about 50 nm. DC Hall effect measurements imply a hole concentration of 4.3×10^{20} cm^{-3}, and SQUID measurements a T_C of 95 K. Unlike as-grown MBE films, Ga$_{1-x}$Mn$_x$As formed by II-PLM do not contain Mn at interstitial sites; instead, non-substitutional Mn atoms are found to be randomly located, perhaps as Mn clusters [8]. Importantly, no evidence of ferromagnetism with T_C above 300 K is found in II-PLM samples, indicating that the ferromagnetic properties are not due to 2nd phases such as MnAs or Ga$_x$Mn$_y$.

3 Experimental Technique

We are reporting Kerr and Faraday measurements in the 1–11 μm (1165–115 meV) range, which characterizes the valence band structure. In this critical wavelength range, free carrier Faraday-rotation is a well known technique for the determination of the carrier effective mass of semiconductors [9] and metals [10]. In p-type GaAs, features associated with transitions between Zeeman split valence sub-bands can be seen in this energy range [11]. For GaMnAs, our theoretical calculations predict strong features due to free holes and transitions between spin-split valence sub-bands [12].

A key advantage of Faraday and Kerr measurements over conventional transmission and reflection measurements is that they also are sensitive to the off-diagonal conductivity σ_{xy}, and thus can be used to determine all components of the magneto-optical conductivity tensor [13]. Furthermore, Faraday and Kerr signals follow the hysteretic behavior of the magnetization, thus allowing the separation of ferromagnetic effects from the paramagnetic response of the substrate or the film.

The Faraday and Kerr angles are measured with a modulation technique using different laser sources [13, 14]. Linearly polarized laser light illuminates the surface of the sample at near-normal incidence, and splits into a reflected and refracted beam. The refracted and reflected beams become elliptically polarized with the major axis rotated with respect to the incident linear laser polarization. The real (imaginary) part of the Faraday angle θ_F represents the rotation (ellipticity) of the transmitted polarization. In transmission measurements, the rotation of the polarization is due to the film's dispersive properties for circularly polarized light while the ellipticity is due to extinction properties. Similarly, the complex Kerr angle θ_K describes the polarization of reflected light.

4 Results

Unlike the longitudinal infrared conductivity σ_{xx}, which in Ga$_{1-x}$Mn$_x$As is dominated by a single broad absorption peak near 250 meV [7, 12, 15] infrared Faraday and Kerr spectra show several features, including sign changes. This additional structure is mainly due to the fact that Faraday and Kerr measurements, which are proportional to the Hall conductivity σ_{xy}, are sensitive to the difference in the sample's optical response for left and right circularly polarized light whereas σ_{xx} measurements probe the sum of the optical responses for these two polarization modes. In Figs. 1 and 2, we plot the Faraday and Kerr spectra, respectively, for the two samples. The values are measured at 10 K and correspond to the magnetization fully saturated. The paramagnetic component was subtracted. The sign convention used is discussed in [13].

In Fig. 1, we have plotted the Faraday rotation Re(θ_F) (a) and ellipticity Im(θ_F) (b) for the two samples as a function of photon energy. As can be seen in Fig. 1a, for both samples Re(θ_F) peaks near 300 meV, changes sign around 600 meV, and reaches a minimum near 800 meV before heading back toward positive values and a second peak near 900–1000 meV. The amplitude of Re(θ_F) is approximately a factor of two larger for the II-PLM, which also shows a much sharper second peak near 900 meV. In Fig. 1b, the Im(θ_F), which is related to the films' circular dichroism, has a single peak near 700 meV that is flanked by two dips,
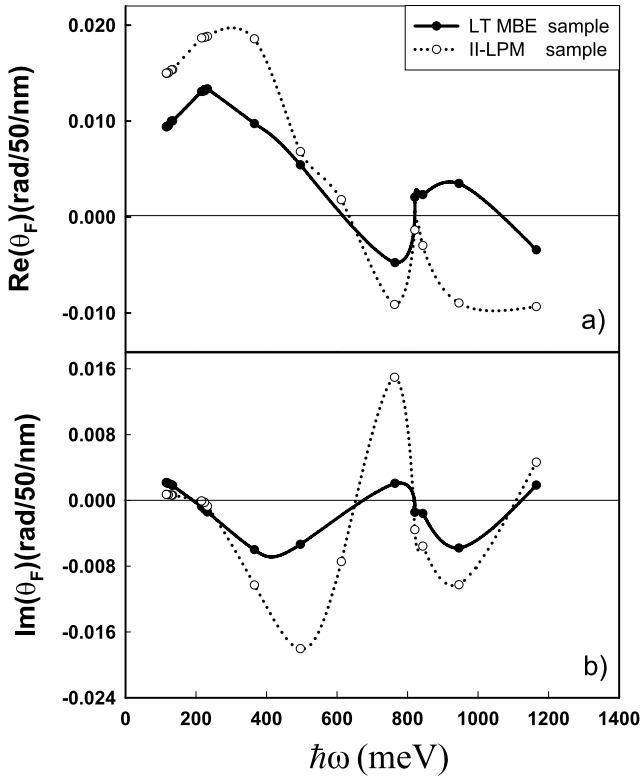
Fig. 1 **a** Faraday rotation, and **b** ellipticity for both the LT-MBE and II-PLM GaMnAs samples as a function of laser frequency. *Lines* are guides to the eye

Fig. 2 **a** Kerr rotation, and **b** ellipticity for both the LT-MBE and II-PLM GaMnAs samples as a function of laser frequency. *Lines* are guides to the eye

one near 500 meV and the other near 900 meV. $Im(\theta_F)$ goes through four sign changes in the 100–1200 meV range. Although the magnitude of $Im(\theta_F)$ is significantly larger for the II-PLM sample, the qualitative behavior for the two samples is remarkably similar.

Figure 2 shows the Kerr rotation $Re(\theta_K)$ (a) and ellipticity $Im(\theta_K)$ (b) for the two samples as a function of photon energy. Except for a reversed sign, the behavior of $Re(\theta_K)$ in Fig. 2a is qualitatively similar to that of $Re(\theta_F)$ in Fig. 1a. $Re(\theta_K)$ dips near 300 meV, approaches positive values, changing sign near 800 meV for the II-PLM sample. Both samples show a weaker dip in $Re(\theta_K)$ near 900 meV and it appears that $Re(\theta_K)$ for the MBE sample will become positive above 1200 meV. Except for a reversed sign, the behavior of $Im(\theta_K)$ is very similar to that of $Im(\theta_F)$. Again, the $Im(\theta_K)$ spectra for the two samples are qualitatively very similar, with the II-PLM sample showing a stronger signal.

Although not shown in Figs. 1 and 2, sign changes in both θ_F and θ_K can be induced at a fixed photon energy by changing temperature. This will be explored in greater depth both experimentally and theoretically in future work.
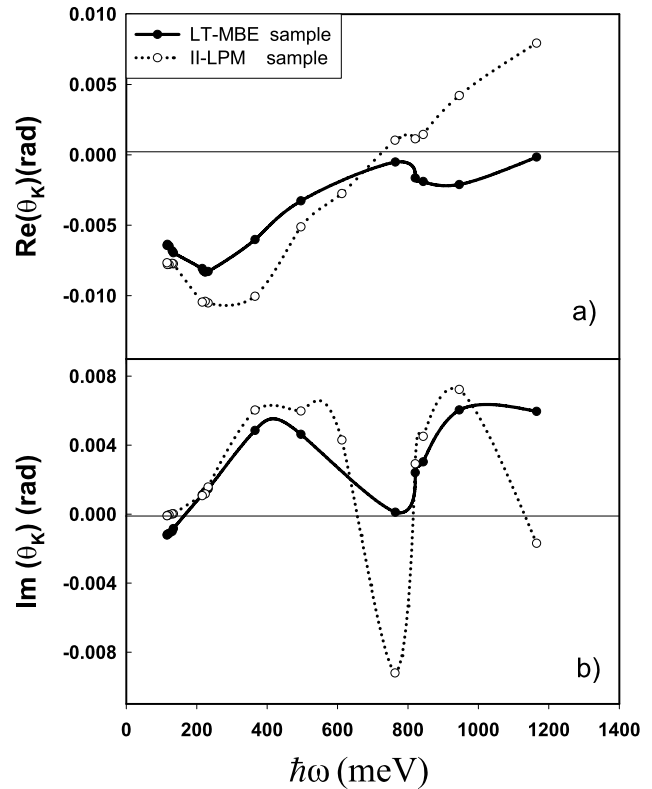
5 Discussion

We now discuss the results within the framework of model calculations [12] based on the itinerant holes assumption, which appears to account for most of the features observed. We start with the ellipticity $Im(\theta)$ (Figs. 1b and 2b), which in transmission is equivalent to magnetic circular dichroism. The ellipticity data shows strong resonance behavior, suggesting that multiple transitions from the Fermi level to higher lying states are involved. Eight band $\vec{k} \cdot \vec{p}$ effective Hamiltonian calculations suggest that the low energy spectrum is due to transitions between the spin-slit valence bands: light hole and heavy hole bands and spin-orbit band to heavy and light hole bands at about 500 meV. Above 800 meV, features associated with the valence band to conduction band appear. Theoretical calculations predict a shift to higher energy of this peak with decreasing hole concentrations due to band narrowing effects. The introduction of defect impurity levels (due to As antisites or Mn interstitials or segregation effects) in the band gap in a ten band model causes strong changes in the calculated ellipticity (see Fig. 7 in [12]). First, a sign change at low energy below 200 meV appears, which is consistent with the experimental results (Figs. 1b and 2b). Also, the low energy peak shifts to

higher energy while the 1 eV energy peak shifts to low energy. This is due to the fact that the ellipticity signal is concentrated around the valence-conduction-band transition for the eight-band model while it is around the valence-defect-band transition for the ten-band calculation. The experimental findings are in qualitative agreement with these calculations showing the importance of deep defect impurities levels in these magneto-optical measurements.

The Faraday and Kerr rotation data in Figs. 1a and 2a show a peak at about 250 meV, a sign change at about 600 meV and a feature at 800 meV, all of which are consistent with the band calculations [12].

6 Conclusion

In spite of the fundamentally different growth techniques of the two samples, the infrared Faraday and Kerr spectra show a remarkable similarity, suggesting that the same transitions are dominating the magneto-optical response at these energies, which are characteristic of the valence band structure. The rich structure that is revealed by infrared Faraday and Kerr measurements opens the possibility of new, more detailed tests of theoretical models. The presence of the deep impurity states in the band gap are necessary in order to account for the Faraday and Kerr features that are observed in the near infrared region ($\sim$1000 meV). A more systematic analysis in which the carrier doping is changed in a single sample, either by annealing or electrical gating is under way. We also are exploring the carrier density dependence by studying a series of samples which are intentionally compensated with donors. Although this work has focused on low temperature measurements, the temperature dependence of the infrared Faraday and Kerr effect is interesting, exhibiting sign changes at fixed photon energy. Combining the energy, temperature, and carrier density dependence of the Faraday and Kerr signals in a detailed comparison with theoretical predictions promises to give a more reliable picture of the nature of the ferromagnetism in this complex material.

References

1. Jungwirth, T., Sinova, J., Masek, J., Kucera, J., MacDonald, A.H.: Rev. Mod. Phys. **78**, 809 (2006)
2. Blinowski, J., Kacman, P.: Phys. Rev. B **67**(12), 121204 (2003)
3. Ando, K., Hayashi, T., Tanaka, M., Twardowski, A.: Appl. Phys. **83**, 6548 (1998)
4. Beschoten, B., Crowell, P.A., Malajovich, I., Awschalom, D.D., Matsukura, F., Shen, A., Ohno, H., Szczytko, J., Mac, W., Twardowski, A., Matsukura, F., Ohno, H.: Phys. Rev. B **59**, 12935 (1999)
5. Hrabovsky, D., Vanelle, E., Fert, A.R., Yee, D.S., Redoules, J.P., Sadowski, J., Kanski, J., Ilver, L.: Appl. Phys. Lett. **81**, 2806 (2002)
6. Lang, R., Winter, A., Pascher, H., Krenn, H., Liu, X., Furdyna, J.K.: Phys. Rev. B **72**, 024430 (2005)
7. Burch, K.S., Shrekenhamer, D.B., Singley, E.J., Stephens, J., Sheu, B.L., Kawakami, R.K., Schiffer, P., Samarth, N., Awshalom, D.D., Basov, D.N.: Phys. Rev. Lett. **97**, 087208 (2006)
8. Scarpulla, M.A., Dubon, O.D., Yu, K.M., Monteiro, O., Pillai, M.R., Aziz, M.J., Ridgway, M.C.: Appl. Phys. Lett. **82**, 1251 (2003)
9. Boswarva, I.M., Howard, R.E., Lidiard, A.B.: Proc. Roy. Soc. Lond. A **269**, 125 (1962)
10. Cerne, J., Schmadel, D.C., Grayson, M., Jenkins, G.S., Simpson, J.R., Drew, H.D.: Phys. Rev. B **61**, 8133 (2000)
11. Lee, T.H., Fan, H.Y.: Phys. Rev. **165**, 927 (1968)
12. Hankiewicz, E.M., Jungwirth, T., Dietl, T., Timm, C., Sinova, J.: Phys. Rev. B **70**, 245211 (2004)
13. Kim, M.-H., Acbas, G., Yang, M.-H., Ohkubo, I., Christen, H., Mandrus, D., Scarpulla, M.A., Dubon, O.D., Schlesinger, Z., Khalifah, P., Cerne, J.: Phys. Rev. B **75**, 214416 (2007)
14. Cerne, J., Schmadel, D.C., Rigal, L., Drew, H.D.: Rev. Sci. Instr. **74**, 4755–4767 (2003)
15. Jungwirth, T., Sinova, J., MacDonald, A.H., Gallagher, B.L., Novak, V., Edmonds, K.W., Rushforth, A.W., Campion, R.P., Foxon, C.T., Eaves, L., Olejnik, K., Masek, J., Eric Yang, S.-R., Wunderlich, J., Gould, C., Molenkamp, L.W., Dietl, T., Ohno, H.: cond-mat, arXiv:0707.0665v2